

Demonstration of Orbital Angular Momentum Multiplexing and Demultiplexing Based on a Metasurface in the Terahertz Band

Huan Zhao,[†] Baogang Quan,[‡] Xinke Wang,[†] Changzhi Gu,[‡] Junjie Li,[‡] and Yan Zhang^{*,†,‡}

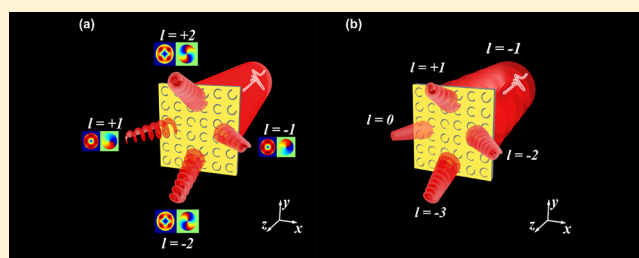
[†]Beijing Key Laboratory of Metamaterials and Devices, Key Laboratory of Terahertz Optoelectronics, Ministry of Education, Beijing Advanced Innovation Center for Imaging Technology, Department of Physics, Capital Normal University, Beijing, 100048, China

[‡]Beijing National Laboratory for Condensed Matter Physics, Institute of Physics, Chinese Academy of Sciences, Beijing, 100190, China

ABSTRACT: Orbital angular momentum of light (OAM) is attracting increasing attention in conjunction with the continuing development of high-speed optical communications. The unlimited nature of OAM allows its multiple degrees of freedom to be used in communications applications. In the OAM multiplexing technique, different OAMs provide independent channels to carry and deliver different data. An OAM multiplexing scheme in the terahertz (THz) band based on use of a single-layer metasurface is demonstrated numerically and experimentally in this work. The designed structure generates four focused phase vortex beams that have

different topological charges under illumination by a Gaussian beam, which means that OAM multiplexing with four channels is realized. When an individual vortex beam is used as the incident light, only one channel is identified and extracted as a focal spot; that is, demultiplexing of the OAM signal is achieved. The structure has subwavelength-level thickness, which enriches the number of potential approaches available for the miniaturization and integration of THz communication systems. The performance of the designed OAM multiplexing and demultiplexing device shows excellent agreement between the theoretical predictions and experimental results, thus indicating that this device is suitable for ultrahigh-speed THz communications.

KEYWORDS: optical angular momentum, metasurface, terahertz, high-speed optical communication



Orbital angular momentum of light (OAM), which is dependent on the spatial distribution of the optical field, is the angular momentum component of a light beam. In the 1990s, it was found that phase vortex beams, which have a phase term that can be described by $\exp(i l \theta)$, have an OAM of $l \hbar$ per photon, where l is the topological charge, θ is the azimuthal angle, and \hbar is Planck's constant h divided by 2π . Another angular momentum property of light is the spin angular momentum (SAM), which is associated with the spin of the photon, and the SAM can be $\pm \hbar$ per photon. The SAM is expressed as a left or right circular polarization.^{1–3} Unlike the SAM, the OAM is unlimited and thus has many more degrees of freedom that can be used. Recently, the OAM has become a research hotspot because of its various applications in fields including optical manipulation, optical trapping, optical tweezers, quantum information processing, and, in particular, high-speed optical communications.^{4–14}

There are two basic methods for use of the OAM in optical communications. Similar to other physical dimensions such as frequency, time, complex amplitude, and polarization, it is possible to use either an OAM modulation scheme or an OAM multiplexing technique. When using the OAM modulation scheme, different data can be encoded into different OAMs. However, in OAM multiplexing, the different OAMs are used as independent channels to carry and deliver the different data.

Therefore, OAM multiplexing offers the potential to increase the transmission capacity and efficiency of communication systems tremendously. Various multiplexing technologies are available in optical communications, including wavelength-division multiplexing (WDM),^{15–17} optical time-division multiplexing (OTDM),¹⁸ polarization-division multiplexing (PDM),^{15–19} space-division multiplexing (SDM),¹⁹ and mode-division multiplexing (MDM).²⁰ These technologies allow users to combine OAM multiplexing with other multiplexing approaches. When OAM multiplexing was combined with PDM, which required use of 16 OAM beams and two polarizations, 2.56 Tbit/s free-space communication was achieved on a single wavelength.²¹ A combination of OAM multiplexing with WDM enabled operation of a 2 Tbit/s data link in free space using two OAM beams at 25 wavelengths²² and 1.6 Tbit/s transmission when using two OAM modes at 10 wavelengths in a vortex fiber.²³ These higher dimensions of combination allow higher communication speeds, and high-speed communication at 100 Tbit/s was achieved over both

Special Issue: Ultra-Capacity Metasurfaces with Low Dimension and High Efficiency

Received: October 1, 2017

Published: October 27, 2017

free space and a special vortex fiber using a combination of OAM multiplexing, WDM, and PDM.²⁴

Terahertz (THz) radiation, which is also known as submillimeter radiation, occupies the middle ground between microwaves and infrared light waves. Because of unique properties such as low photon energy and high penetrability, THz radiation can be used in a wide range of applications including security checks, medical examinations, astronomy, and communications. THz radiation can also be used as a carrier for ultrahigh-speed communications. It has been demonstrated that a THz emitter has a 50 Gbit/s data transfer speed and approaches a Tbit/s rate when using a simple single communication channel.^{25,26} To further increase THz communication speeds, multiplexing technology must be adopted. However, because of the longer wavelength properties of THz radiation, the component required for THz radiation modulation is quite large and blocks integration of the THz communication system. Recently, the emerging technology of metasurfaces, which are composed of arrays of subwavelength antennas, has demonstrated attractive properties for potential applications, including small size, light weight, and low cost. Metasurfaces have been applied to shaping of wavefronts of light by introducing an abrupt interfacial phase discontinuity between the visible and microwave frequencies.^{27–30} By modulating both the phase and the amplitude of the electromagnetic waves, metasurfaces can easily be used to generate phase vortex beams.^{31–34} The integration of OAM multiplexing with SDM, WDM, and PDM into a single ultrathin metasurface for operation in the visible light band has been achieved in numerical simulations.³⁵ An ultrathin nanostructured OAM generator with multiple focal planes along its longitudinal direction has been realized for operation in the visible light band, which achieved OAM multiplexing experimentally along the propagation direction.³⁶ However, the distributions of the different OAM patterns along the propagation direction will lead to difficulties in multiplexing. Moreover, an ultrathin optical device that can simultaneously realize a polarization-controllable hologram and superposition of OAM in multiple channels was experimentally demonstrated in the visible light band. By continuously controlling the polarization state of the incident light, the polarization-dependent holographic images in two channels along the horizontal direction and the continuous control of OAM superposition in two channels along the vertical direction are realized.³⁷ However, OAM generation and multiplexing devices for operation in the THz band that can integrate and miniaturize a THz communication system have not been realized to date.

In this paper, OAM multiplexing in the THz band based on a single-layer metasurface has been demonstrated both numerically and experimentally. The designed structure can generate four focused phase vortex beams with different topological charges under an incident Gaussian beam, which means that it can then realize OAM multiplexing with four channels. When using each of the individual vortex beams as incident beams, only one channel will be identified and extracted at the focal spot; that is, OAM demultiplexing was also achieved. The fabricated structure has dimensions of approximately $1.0 \times 1.0 \text{ cm}^2$, and its thickness is on the subwavelength scale, which will enrich the range of approaches that can be used for miniaturization and integration of THz communication systems. The performances of the designed OAM multiplexing and demultiplexing devices show excellent agreement between

the theoretical predictions and the experimental results, which indicates that this approach will be useful for ultrahigh-speed THz communications device design.

DESIGN

As shown in Figure 1a, when an x -polarized THz Gaussian wave was used as the incident beam, four vortex beams with

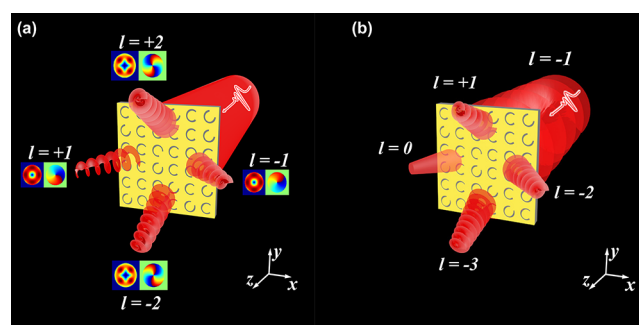


Figure 1. Schematics of (a) OAM multiplexing and (b) OAM demultiplexing.

different topological charges were scattered in four different directions. The focused vortex beams with topological charges of $l = +1, -1, +2,$ and -2 corresponded to the tilt directions along the $-x$ -, $+x$ -, $+y$ -, and $-y$ -axes, respectively, which means that the designed structure can achieve OAM multiplexing. When a vortex beam with one of the topological charges of $l = +1, -1, +2,$ or -2 impinges on the structure, the predesigned vortex beam with the inverse topological charge counteracts this beam to generate a focal spot (i.e., if the incident beam is a vortex beam with $l = -1$, a focal spot will be generated with tilt along the $-x$ direction), as shown in Figure 1b; this means that OAM demultiplexing has been realized.

The basic antenna structure is shown in Figure 2a and consists of a C-shaped slot on a gold sheet and a substrate composed of a $500\text{-}\mu\text{m}$ -thick double-side-polished high-resistivity silicon wafer. When a linearly polarized electromagnetic wave impinges on the antenna unit, both symmetric and antisymmetric modes can be excited and a cross-polarized field is then scattered by these two modes. The amplitude and phase of the re-emitted field can then be modulated by adjusting the geometrical parameters of the antennas. The antenna parameters are indicated in Figure 2a. P is the antenna period, which is $100 \mu\text{m}$. R and r are the outer and inner radii of the C-shaped slot and are 40 and $30 \mu\text{m}$, respectively. The azimuth angle α of the C-shaped slot is defined as the angle between the symmetric axis of the slot and the x -axis, while β is the opening angle of the split. Sixteen antennas were used to realize phase modulation of the cross-polarized wave over the range from 0 to 2π with identical amplitude modulation at the operating frequency of 0.8 THz . The first eight antennas are shown in Figure 2b; the azimuth angle for each of these antennas is $\alpha = 45^\circ$ and their opening angles are $\beta = 5^\circ, 17^\circ, 30^\circ, 45^\circ, 70^\circ, 115^\circ, 135^\circ,$ and 145° . The other eight antennas have the same range of opening angles as the first eight antennas but an azimuth angle α of -45° . Using these 16 antennas, the phase modulation of the transmitted cross-polarized THz wave can reach 2π with a constant phase difference of $\pi/4$, while the amplitude transmission is maintained at approximately 22% at the operating frequency of 0.8 THz , as shown in Figure 2c. The amplitude transmission

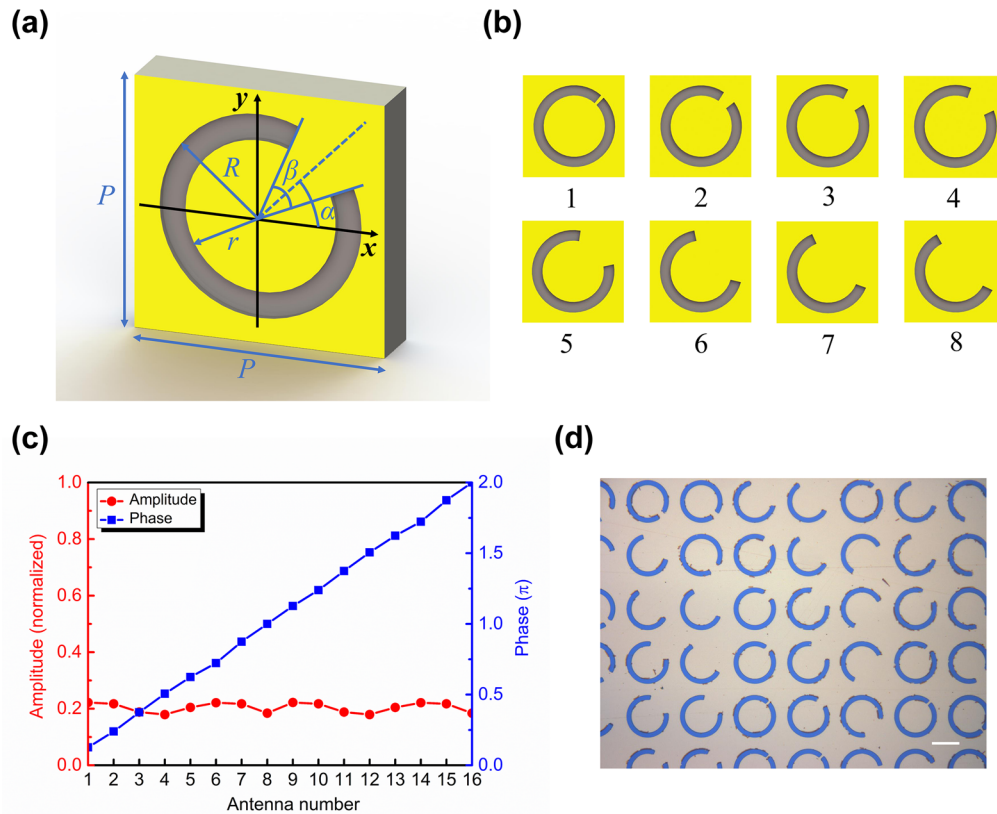


Figure 2. (a) Schematic view of an antenna unit. The antenna period is $P = 100 \mu\text{m}$. The outer and inner radii of the C-shaped slot are $R = 40 \mu\text{m}$ and $r = 30 \mu\text{m}$, respectively. α is the azimuth angle of the C-shaped slot, while β is the opening angle of the split. (b) Top view of the first eight antennas, which have $\alpha = 45^\circ$ and opening angles of $\beta = 5^\circ, 17^\circ, 30^\circ, 45^\circ, 70^\circ, 115^\circ, 135^\circ,$ and 145° . The other eight antennas have the same opening angles as the first eight antennas but have an azimuth angle of $\alpha = -45^\circ$. (c) Simulated scattering amplitudes and phases of cross-polarized radiation from the individual antenna unit at 0.8 THz. (d) Micrograph of the fabricated structure, where the scale bar represents $50 \mu\text{m}$.

is not so good because of the low polarization conversion efficiency of the single-layer gold antenna; one may use a multilayer metasurface or dielectric metasurface to improve the efficiency.^{38,39} The antenna parameters and the modulation results were obtained by appropriate simulations using commercial FDTD Solutions simulation software based on the finite-difference time-domain method. The antenna unit shown in Figure 2a was constructed as the model for the simulations. Periodic boundary conditions were applied in both the x and y directions, while perfectly matched layers are used as the boundary condition in the propagation direction. The refractive index of the silicon wafer is determined to be 3.4 in the simulation. The device is composed of 100×100 antenna units and was fabricated using a combination of vacuum evaporation, photolithography, and a subsequent deposition process. An image of part of the sample is shown in Figure 2d and shows that the C-shaped slots were fabricated well.

To obtain the phase profile expected for multiplexing of four OAMs, the phase distributions of each of the vortex beams are superposed with the tilt phase distributions for the four different directions along the $\pm x$ and $\pm y$ directions. The vortex phase distributions with the different values of topological charge l can be described as functions of their positions as follows:

$$\varphi_l(x, y) = l \arctan\left(\frac{y}{x}\right), \quad l = \pm 1, \pm 2 \quad (1)$$

The phase distributions of the four tilt wavefronts are described as follows:

$$\begin{aligned} \varphi_{\pm x}(x) &= \pm \frac{2\pi}{D}x, \\ \varphi_{\pm y}(y) &= \pm \frac{2\pi}{D}y \end{aligned} \quad (2)$$

where $D = 3200 \mu\text{m}$ is the super-unit-cell period along the phase gradient direction. Under normal incidence, the angle of refraction can be calculated to be $\theta_t = 6.7^\circ$.

We superposed the vortex phase distributions and the tilt phase distributions as follows:

$$\begin{aligned} \varphi_1(x, y) &= \varphi_{-1} + \varphi_{+x} = -\arctan\left(\frac{y}{x}\right) + \frac{2\pi}{D}x, \\ \varphi_2(x, y) &= \varphi_{+1} + \varphi_{-x} = \arctan\left(\frac{y}{x}\right) - \frac{2\pi}{D}x, \\ \varphi_3(x, y) &= \varphi_{+2} + \varphi_{+y} = 2 \arctan\left(\frac{y}{x}\right) + \frac{2\pi}{D}y, \\ \varphi_4(x, y) &= \varphi_{-2} + \varphi_{-y} = -2 \arctan\left(\frac{y}{x}\right) - \frac{2\pi}{D}y \end{aligned} \quad (3)$$

These four phase distributions are then arranged in the device. The device is composed of 100×100 antenna units, and the cell in the n th row and the m th column thus has the following phase distribution:

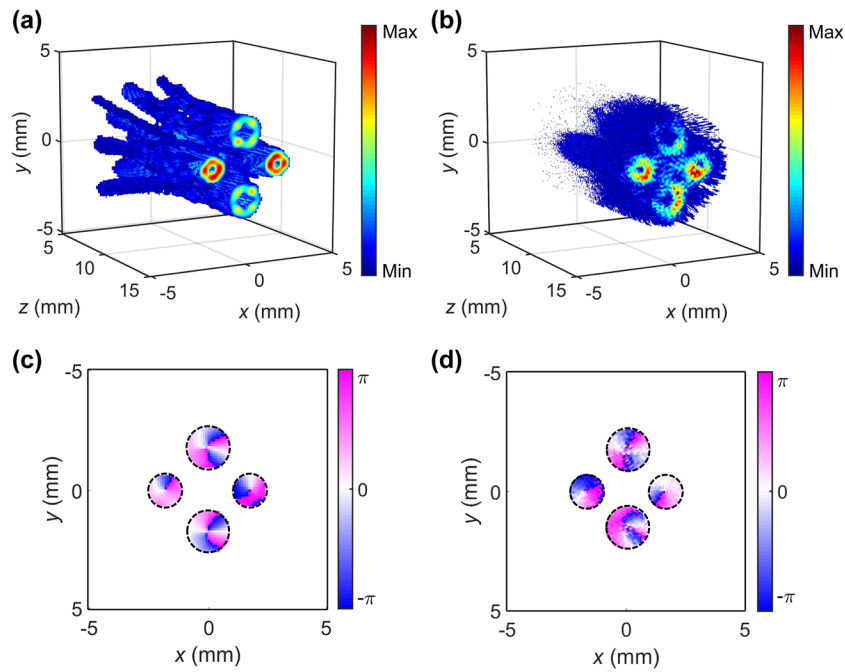


Figure 3. Results of OAM multiplexing. (a, b) Simulated and experimental amplitude distributions of the z-scan. (c, d) Simulated and experimental phase profiles at the predesigned focal plane, which is located at $z = 15$ mm.

$$\varphi_{m,n}(x, y) = \begin{cases} \varphi_1(x, y), & m = 2p - 1, n = 2q - 1, \\ \varphi_2(x, y), & m = 2p, n = 2q - 1, \\ \varphi_3(x, y), & m = 2p - 1, n = 2q, \\ \varphi_4(x, y), & m = 2p, n = 2q \end{cases} \quad (4)$$

where p and q are integers in the range from 1 to 50. Finally, the phase distribution of a focusing lens is attached to focus the vortex beam that has been generated on the focal plane. The phase distribution of the focusing lens can then be obtained based on the equal optical path principle, as follows:

$$\varphi(x, y) = \frac{2\pi}{\lambda} (f - \sqrt{x^2 + y^2 + z^2}) \quad (5)$$

where f is the focal length of the lens, which is set at 15 mm, and $\lambda = 375 \mu\text{m}$ is the working wavelength. The phase value is wrapped within the range from 0 to 2π and is then quantized into 16 values. Based on the Fourier transform characteristics, the tilt wavefront will cause a shift at the lens focal plane; the center of the generated vortex beam will therefore be shifted from the coordinate origin. The designed shift in the focal spot from the coordinate origin can be calculated as follows:

$$\begin{aligned} \Delta x_f &= f \sin \theta_t \approx f \tan \theta_t = \pm f \frac{\lambda}{D} \\ \Delta y_f &= f \sin \theta_t \approx f \tan \theta_t = \pm f \frac{\lambda}{D} \end{aligned} \quad (6)$$

RESULTS AND DISCUSSION

To investigate the OAM multiplexing properties of the designed structure during propagation, z-scan measurements were performed by simply moving the structure along the z-axis. The distance between the structure and the probe crystal is varied from 5 mm to 15 mm in steps of 0.1 mm. The amplitude

distributions measured along the z-axis are shown in Figure 3b, while the simulated results are shown in Figure 3a; the amplitude distributions of all vortex beams had preformed doughnut shapes, but the square-shaped modulation was attributed to the square aperture shape of the structure. The nonuniformity on the ring is caused by the transmission discrepancy. As one can see, the image quality is not so good; this is attributed to the limited cell numbers, which were restricted by the inherent major wavelength of THz waves and the small imaging area of the experimental setup. Figure 3c and d show the phase profiles that were obtained numerically and experimentally, respectively. Figure 3d shows that four vortex beams with different topological charges were generated with almost identical phase profiles to those of the simulated results at the predesigned positions. The measured positions and the relative errors for each of the generated vortex beams are shown in Table 1, which shows that the relative errors at all positions

Table 1. Measured Positions and Relative Errors for Each Vortex Beam Generated during OAM Multiplexing

l^a	x^b [mm]	y [mm]	relative error [%]
1	-1.73	0	1.1
-1	1.67	0	4.5
2	0	1.65	5.7
-2	0	-1.58	9.7

^aTopological charge. ^bThe calculated distance for all vortex beams was 1.76 mm.

are less than 10%. All the measured amplitude distributions and phase profiles coincided with the simulated results, which indicated that the designed structure achieved OAM multiplexing with four channels.

To demonstrate OAM demultiplexing, four vortex phase plates were fabricated to generate the required vortex beams with topological charges of $l = +1, -1, +2,$ and -2 . Figure 4c and d show the amplitude distributions for incident vortex

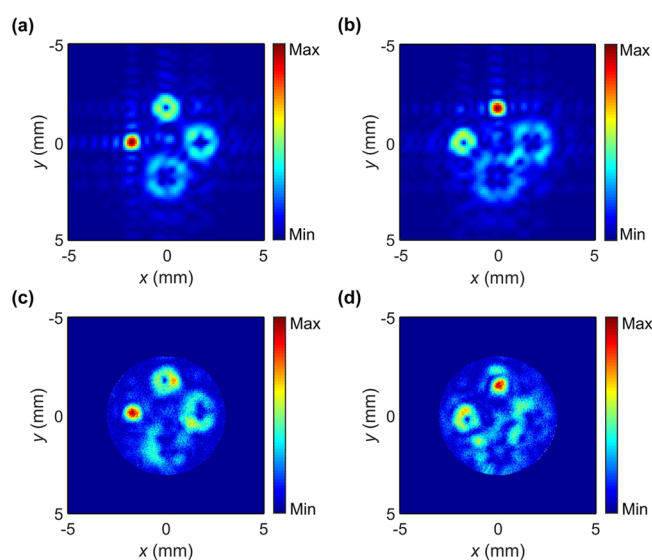


Figure 4. Results of OAM demultiplexing. (a, b) Simulated amplitude distribution at the predesigned focal plane, which is located at $z = 15$ mm, for incident light composed of vortex beams with $l = -1$ and $l = -2$, respectively. (c, d) Experimental results corresponding to (a) and (b), respectively.

beams with $l = -1$ and $l = -2$, respectively. The corresponding simulated results are shown in Figure 4a and b, respectively. When the vortex beam with $l = -1$ was used as the incident light, a focal spot with a Gaussian amplitude distribution was generated at $x = -1.71$ mm, $y = 0$ mm, with a relative distance error of 2.2%; when the vortex beam with $l = -2$ was used as the incident light, the focal spot was generated at $x = 0$ mm, $y = 1.69$ mm, with a relative distance error of 3.4%. When the other two vortex beams were used as the incident light, similar results were obtained, which means that the designed structure realized OAM demultiplexing.

CONCLUSIONS

In conclusion, OAM multiplexing and demultiplexing based on use of a single metasurface has been demonstrated numerically and experimentally. The designed structure realized four individual OAM multiplexing channels under an incident Gaussian beam; then, when each individual vortex beam was used as an incident beam, one corresponding channel was identified and extracted in the form of a focal spot, and thus OAM demultiplexing was achieved. Four OAM channels were generated based on the design method; if one wants more multiplexing channels, the method based on Damman gratings^{31,40} may be used to improve the communication capacity. The performances of the designed OAM multiplexing and demultiplexing devices showed excellent agreement between the theoretical predictions and experimental results, which indicated that this approach will be useful in the design of ultrahigh-speed THz communication devices.

METHODS

In the experiments, a THz holographic imaging system^{41,42} was used to characterize the performance of the designed structure. A schematic of part of the experimental setup is shown in Figure 5. The light source was a 100 fs ultrashort laser pulse with an 8 mm spot diameter, an 800 nm central wavelength, and a 1 kHz repetition rate that was produced by a Ti:sapphire regenerative amplifier. The laser beam, which had an average

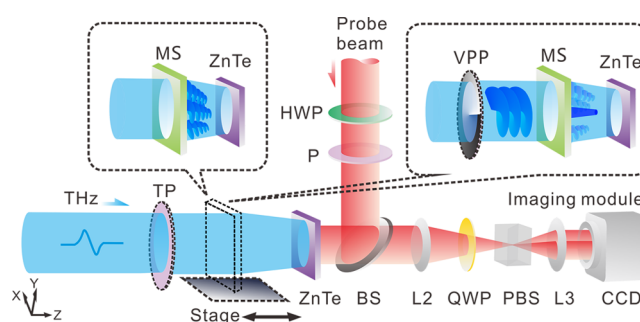


Figure 5. Experimental setup used for performance characterization of the designed structure (HWP: half-wave plate; P: polarizer; TP: THz polarizer; MS: metasurface structure; VPP: vortex phase plate; BS: beam splitter; QWP: quarter-wave plate; PBS: polarizing beam splitter).

power of 900 mW, was divided into two parts, which were then used as the pump (880 mW) and probe (20 mW) beams required for generation and detection of the THz waves, respectively. The pump beam impinged upon a 1-mm-thick $\langle 110 \rangle$ ZnTe crystal to generate the THz beam via the optical rectification effect. The horizontally polarized (x -polarized) THz beam, which had a diameter of 24 mm, passed through a THz polarizer to maintain its polarization before impinging on the structure, and the scattered vertically polarized (y -polarized) THz beam was detected using another $\langle 110 \rangle$ ZnTe crystal. In the probe optical path, a half-wave plate and a polarizer were used to modulate the probe beam polarization. The probe beam with the y -polarization was then reflected by a nonpolarizing beam splitter (T:R = 5:5) toward the sensor crystal. In the sensor crystal, the polarization of the probe beam was modulated by the THz field via the Pockels effect, and the reflected probe beam was then captured using the imaging unit. The imaging unit consisted of a 4f system (two convex lenses, denoted by L2 and L3), a quarter-wave plate, a polarized beam splitter (PBS), and a charge-coupled device (CCD) camera. The PBS was used to split the probe beam into two beams with orthogonal polarizations, and the two images of the sensor crystal were then projected onto the CCD camera by the 4f system. The THz complex field could then be extracted using the balanced electro-optic detection technique. By varying the optical path difference between the THz beam and the probe beam, 100 temporal images could be captured at each time delay with a time window of 17 ps. The amplitude and phase information at the different frequencies could then be extracted by performing Fourier transformations on the temporal signals that occurred at each pixel.

AUTHOR INFORMATION

Corresponding Author

*E-mail: yzhang@cnu.edu.cn.

ORCID

Junjie Li: 0000-0002-1508-9891

Yan Zhang: 0000-0001-9235-6861

Notes

The authors declare no competing financial interest.

ACKNOWLEDGMENTS

This work was supported by the 973 Program of China (grant no. 2013CBA01702); the National Key R&D Program of China (grant nos. 2016YFA0200800, 2016YFA0200400, and

2016YFB0100500); the National Natural Science Foundation of China (grant nos. 11474206, 11374216, 11404224, 1174243, 91323304, 11674387, 11574385, and 11774246); the Beijing Youth Top-Notch Talent Training Plan (CIT&TCD 201504080); the Beijing Nova Program (grant no. Z161100004916100); and the Scientific Research Base Development Program of the Beijing Municipal Commission of Education.

REFERENCES

- (1) Poynting, J. H. The wave motion of a revolving shaft, and a suggestion as to the angular momentum in a beam of circularly polarised light. *Proc. R. Soc. London, Ser. A* **1909**, *82*, 560–567.
- (2) Beth, R. A. Mechanical detection and measurement of the angular momentum of light. *Phys. Rev.* **1936**, *50*, 115–125.
- (3) Allen, L.; Beijersbergen, M. W.; Spreeuw, R. C.; Woerdman, J. P. Orbital angular momentum of light and the transformation of Laguerre-Gaussian laser modes. *Phys. Rev. A: At., Mol., Opt. Phys.* **1992**, *45*, 8185–8189.
- (4) Dholakia, K.; Cizmar, T. Shaping the future of manipulation. *Nat. Photonics* **2011**, *5*, 335–342.
- (5) Paterson, L.; Macdonald, M. P.; Arlt, J.; Sibbett, W.; Bryant, P. E.; Dholakia, K. Controlled rotation of optically trapped microscopic particles. *Science* **2001**, *292*, 912–914.
- (6) Macdonald, M. P.; Paterson, L.; Volke-Sepulveda, K.; Arlt, J.; Sibbett, W.; Bryant, P. E.; Dholakia, K. Creation and manipulation of three-dimensional optically trapped structures. *Science* **2002**, *296*, 1101–1103.
- (7) Padgett, M.; Bowman, R. Tweezers with a twist. *Nat. Photonics* **2011**, *5*, 343–348.
- (8) Bernet, S.; Jesacher, A.; Fürhapter, S.; Maurer, C.; Ritsch-Marte, M. Quantitative imaging of complex samples by spiral phase contrast microscopy. *Opt. Express* **2006**, *14*, 3792–3805.
- (9) Mair, A.; Vaziri, A.; Weihs, G.; Zeilinger, A. Entanglement of the orbital angular momentum states of photons. *Nature* **2001**, *412*, 313–316.
- (10) Nagali, E.; Sansoni, L.; Sciarrino, F.; Martini, F. D.; Marrucci, L.; Piccirillo, B.; Karimi, E.; Santamato, E. Optimal quantum cloning of orbital angular momentum photon qubits through hong-ou-mandel coalescence. *Nat. Photonics* **2009**, *3*, 720–723.
- (11) Leach, J.; Jack, B.; Romero, J.; Jha, A.; Yao, A. M.; Franke-Arnold, S.; Ireland, D. G.; Boyd, R. W.; Barnett, S. M.; Padgett, M. J. Quantum correlations in optical angle-orbital angular momentum variables. *Science* **2010**, *329*, 662–665.
- (12) Wang, J. Advances in communications using optical vortices. *Photonics Res.* **2016**, *4*, B14–B28.
- (13) Wang, J.; Yang, J. Y.; Fazal, I. M.; Ahmed, N.; Yan, Y.; Huang, H.; Ren, Y. X.; Yue, Y.; Dolinar, S.; Tur, M.; Willner, A. E. Terabit free-space data transmission employing orbital angular momentum multiplexing. *Nat. Photonics* **2012**, *6*, 488–496.
- (14) Chen, P.; Ge, S. J.; Ma, L. L.; Hu, W.; Chigrinov, V.; Lu, Y. Q. Generation of equal-energy orbital angular momentum beams via photopatterned liquid crystals. *Phys. Rev. Appl.* **2016**, *5*, 044009.
- (15) Gnauck, A. H.; Winzer, P. J.; Chandrasekhar, S.; Liu, X.; Zhu, B.; Peckham, D. W. Spectrally efficient long-haul WDM transmission using 224-Gb/s polarization-multiplexed 16-QAM. *J. Lightwave Technol.* **2011**, *29*, 373.
- (16) Zhou, X.; Yu, J. J.; Huang, M. F.; Shao, Y.; Wang, T.; Nelson, L.; Magill, P.; Birk, M.; Borel, P. I.; Peckham, D. W.; Lingle, R.; Zhu, B. Y. 64-Tb/s, 8 b/s/Hz, PDM-36QAM transmission over 320 km using both pre- and post-transmission digital signal processing. *J. Lightwave Technol.* **2011**, *29*, 571–577.
- (17) Sano, A.; Masuda, H.; Kobayashi, T.; Fujiwara, M.; Horikoshi, K.; Yoshida, E.; Miyamoto, Y.; Matsui, M.; Mizoguchi, M.; Yamazaki, H.; Sakamaki, Y.; Ishii, H. Ultra-high capacity WDM transmission using spectrally-efficient PDM 16-QAM modulation and C- and extended L-band wideband optical amplification. *J. Lightwave Technol.* **2011**, *29*, 578–586.
- (18) Richter, T.; Palushani, E.; Schmidt-Langhorst, C.; Ludwig, R.; Molle, L.; Nölle, M.; Schubert, C. Transmission of single-channel 16-QAM data signals at terabaud symbol rates. *J. Lightwave Technol.* **2012**, *30*, 504–511.
- (19) Liu, X.; Chandrasekhar, S.; Chen, X.; Winzer, P. J.; Pan, Y.; Taunay, T. F.; Zhu, B.; Fishteyn, M.; Yan, M. F.; Fini, J. M.; Monberg, E. M.; Dimarcello, F. V. 1.12-Tb/s 32-QAM-OFDM superchannel with 8.6-b/s/Hz intrachannel spectral efficiency and space-division multiplexed transmission with 60-b/s/Hz aggregate spectral efficiency. *Opt. Express* **2011**, *19*, B958–B964.
- (20) Roland, R.; Sebastian, R.; Alan, G.; Cristian, B.; Alberto, S.; Sami, M.; Mina, E.; Ellsworth, B.; René-Jean, E.; Peter, W.; David, P.; Alan, M.; Robert, L. Mode-division multiplexing over 96 km of few-mode fiber using coherent 6×6 MIMO processing. *J. Lightwave Technol.* **2012**, *30*, 521–531.
- (21) Gibson, G.; Courtial, J.; Padgett, M.; Vasnetsov, M.; Pasko, V.; Barnett, S. M.; Arnold, S. F. Free-space information transfer using light beams carrying orbital angular momentum. *Opt. Express* **2004**, *12*, 5448–5456.
- (22) Fazal, I.; Ahmed, N.; Wang, J.; Yang, J. Y.; Yan, Y.; Shamee, B.; Huang, H.; Yue, Y.; Dolinar, S.; Tur, M.; Willner, A. E. 2 Tbit/s free-space data transmission on two orthogonal orbital-angular-momentum beams each carrying 25 WDM channels. *Opt. Lett.* **2012**, *37*, 4753–4755.
- (23) Bozinovic, N.; Yue, Y.; Ren, Y.; Tur, M.; Kristensen, P.; Huang, H.; Willner, A.; Ramachandran, S. Terabit-scale orbital angular momentum mode division multiplexing in fibers. *Science* **2013**, *340*, 1545–1548.
- (24) Huang, H.; Xie, G. D.; Yan, Y.; Ahmed, N.; Ren, Y. X.; Yue, Y.; Rogawski, D.; Willner, M. J.; Erkmén, B. I.; Birnbaum, K. M.; Dolinar, S. J.; Lavery, P. J.; Padgett, M. J.; Tur, M.; Willner, A. E. 100 Tbit/s free-space data link enabled by three-dimensional multiplexing of orbital angular momentum, polarization, and wavelength. *Opt. Lett.* **2014**, *39*, 197.
- (25) Fujishima, M.; Amakawa, S. Recent progress and prospects of terahertz CMOS. *IEICE. Electron. Express* **2015**, *12*, 1–7.
- (26) Fujishima, M.; Amakawa, S.; Takano, K.; Katayama, K.; Yoshida, T. Terahertz CMOS design for low-power and high-speed wireless communication. *IEICE. Trans. Electron.* **2015**, *E98-C*, 1091–1104.
- (27) Yu, N. F.; Genevet, P.; Kats, M. A.; Aieta, F.; Tietienne, J. P.; Capasso, F.; Gaburro, Z. Light propagation with phase discontinuities: generalized laws of reflection and refraction. *Science* **2011**, *334*, 333–337.
- (28) Ni, X. J.; Emani, N. K.; Kildishev, A. V.; Boltasseva, A.; Shalaev, V. M. Broadband light bending with plasmonic nanoantennas. *Science* **2012**, *335*, 427.
- (29) Yin, X. B.; Ye, Z. L.; Rho, J.; Wang, Y.; Zhang, X. Photonic spin hall effect at metasurfaces. *Science* **2013**, *339*, 1405–1407.
- (30) Hu, D.; Wang, X. K.; Feng, S. F.; Ye, J. S.; Sun, W. F.; Kan, Q.; Klar, P. J.; Zhang, Y. Ultrathin terahertz planar elements. *Adv. Opt. Mater.* **2013**, *1*, 186–191.
- (31) Liu, J. P.; Min, C. J.; Lei, T.; Du, L. P.; Yuan, Y. S.; Wei, S. B.; Wang, Y. P.; Yuan, X. C. Generation and detection of broadband multi-channel orbital angular momentum by micrometer-scale meta-reflectarray. *Opt. Express* **2016**, *24*, 212–218.
- (32) He, J. W.; Wang, X. K.; Hu, D.; Ye, J. S.; Feng, S. F.; Kan, Q.; Zhang, Y. Generation and evolution of the terahertz vortex beam. *Opt. Express* **2013**, *21*, 20230–20239.
- (33) Guo, Y. H.; Yan, L. S.; Pan, W.; Luo, B. Generation and manipulation of orbital angular momentum by all-dielectric metasurfaces. *Plasmonics* **2016**, *11*, 337–344.
- (34) Yue, F. Y.; Wen, D. D.; Zhang, C. M.; Gerardot, B. D.; Wang, W.; Zhang, S.; Chen, X. Z. Multichannel polarization-controllable superpositions of orbital angular momentum states. *Adv. Mater.* **2017**, *29*, 1–6.
- (35) Li, Y.; Li, X.; Chen, L. W.; Pu, M. B.; Jin, J. J.; Hong, M. H.; Luo, X. G. Orbital angular momentum multiplexing and demultiplexing by a single metasurface. *Adv. Opt. Mater.* **2017**, *5*, 1600502.

(36) Mehmood, M. Q.; Mei, S. T.; Hussain, S.; Huang, K.; Siew, S. Y.; Zhang, L.; Zhang, T. H.; Ling, X. H.; Liu, H.; Teng, J. H.; Danner, A.; Zhang, S.; Qiu, C. W. Visible-frequency metasurface for structuring and spatially multiplexing optical vortices. *Adv. Mater.* **2016**, *28*, 2533–2539.

(37) Zhang, C. M.; Yue, F. Y.; Wen, D. D.; Chen, M.; Zhang, Z. R.; Wang, W.; Chen, X. Z. Multichannel metasurface for simultaneous control of holograms and twisted light beams. *ACS Photonics* **2017**, *4*, 1906–1912.

(38) Grady, N. K.; Heyes, J. E.; Dibakar, R. C.; Zeng, Y.; Reiten, M. T.; Azad, K. A.; Taylor, A. J.; Dalvit, D. A.; Chen, H. T. Terahertz metamaterials for linear polarization conversion and anomalous refraction. *Science* **2013**, *340*, 1304.

(39) Amir, A.; Yu, H.; Mahmood, B.; Andrei, F. Dielectric metasurfaces for complete control of phase and polarization with subwavelength spatial resolution and high transmission. *Nat. Nanotechnol.* **2015**, *10*, 937.

(40) Chen, P.; Ge, S. J.; Duan, W.; Wei, B. Y.; Cui, G. X.; Hu, W.; Lu, Y. Q. Digitalized geometric phases for parallel optical spin and orbital angular momentum encoding. *ACS Photonics* **2017**, *4*, 1333–1338.

(41) Wang, X. K.; Cui, Y.; Sun, W. F.; Ye, J. S.; Zhang, Y. Terahertz polarization real-time imaging based on balanced electro-optic detection. *J. Opt. Soc. Am. A* **2010**, *27*, 2387–2393.

(42) Wang, X. K.; Cui, Y.; Sun, W. F.; Ye, J. S.; Zhang, Y. Terahertz real-time imaging with balanced electro-optic detection. *Opt. Commun.* **2010**, *283*, 4626–4632.